Monthly Notices of the ROYAL ASTRONOMICAL SOCIETY

MNRAS **499,** 5075–5089 (2020) doi:10.1093/mnras/staa3157
Advance Access publication 2020 October 14

Satellite measurements of artificial light at night: aerosol effects

S. Cavazzani,[1,2]★ S. Ortolani,[1,2] A. Bertolo,[3] R. Binotto,[3] P. Fiorentin,[4] G. Carraro [1] and V. Zitelli[5]

[1]*Department of Physics and Astronomy, University of Padova, Vicolo dell'Osservatorio 3, I-35122 Padova, Italy*
[2]*INAF – Osservatorio Astronomico di Padova, Vicolo dell'Osservatorio 5, I-35122 Padova, Italy*
[3]*Regional Environmental Prevention and Protection Agency of Veneto, Via Ospedale Civile 24, I-35121 Padova, Italy*
[4]*Department of Industrial Engineering, University of Padova, Via Gradenigo 6a, I-35131 Padova, Italy*
[5]*INAF-OAS Osservatorio di Astrofisica e Scienza dello Spazio di Bologna, Via Gobetti 93/3, I-40129 Bologna, Italy*

Accepted 2020 October 7. Received 2020 September 20; in original form 2020 July 22

ABSTRACT

The study of artificial light at night (ALAN) by satellite is very important for the analysis of new astronomical sites and for the long-term temporal evolution observation of the emission from the ground. The analysis of satellite data presents many advantages but also some critical points because of fluctuations in measurements. The main result of this paper is the discovery of a correlation between these fluctuations and the aerosol concentration combined with cloud cover and lunar cycles. In this work, we also present a mathematical empirical model for the light pollution propagation study in relation to the aerosol concentration detected by satellite. We apply this model to the astronomical site of Asiago (Ekar Observatory) providing a possible explanation for the temporal ALAN fluctuations detected by satellite. Finally, we validate the results with the ground collected data.

Key words: atmospheric effects – instrumentation: detectors – light pollution – site testing.

1 INTRODUCTION

Artificial light at night (ALAN) increases the night sky brightness (NSB), creating the most visible effect of light pollution and in particular influencing the astronomical observations in contaminated sites. In the last decades the light pollution has become a global scale and interdisciplinary phenomenon (Kyba et al. 2015) as shown by the growing interest from scientists from various fields of astronomy (Patat 2008; Puschnig, Posch & Uttenthaler 2014; Zhang et al. 2016), ecology, biology (Holker et al. 2010; Gaston et al. 2013; Manfrin et al. 2017), and medicine (Kloog et al. 2009; Stevens et al. 2013). There is a rapidly growing literature on the subject (Mulder et al. 2015). NSB is produced by two main components: the natural component, in turn divided into terrestrial and extraterrestrial, and the artificial component caused by human activities (ALAN). We analyse the Visible Infrared Imaging Radiometer Suite (VIIRS) satellite data for the Veneto (Italy), analysing in particular the site of Padua and Asiago (see Table 1 and Fig. 1). Fig. 1 shows the location of the analysed site developed through the Interactive Data Language (IDL) from VIIRS data. Left-hand panel is the two-dimensional reconstruction and the right-hand panel is the three-dimensional reconstruction of the light emission from the ground at Veneto region (Italy) in 2019 January. The image is a matrix of 700 × 550 pixels corresponding to 140 × 110 km, the colours of the bar above the left-hand panel define the satellite counts processed with IDL.

The VIIRS data detect night clouds, auroras, and airglow thanks to the high signal-to-noise ratio at low radiance levels (Miller et al. 2013; Elvidge et al. 2017). The time series study produced several papers for the calibration of satellite data and the explanation of the satellite count fluctuations. These are based on the various satellite models, the different orbit inclinations, and the satellite angle of view (Coesfeld et al. 2020; Cox et al. 2020; Sanchez de Sanchez et al. 2020).

In this work we try to study these fluctuations through a new approach: we compare the main periodicities of the aerosols and the cloud cover with the lunar cycle at a site highly aerosol contaminated. The free data provided by VIIRS for the years analysed are monthly averages.[1] The averages are calculated on clear nights. The use of satellite data allows a long-term data archive. In this analysis, we analysed the trend of the light emission detected by VIIRS from 2012 to 2019. These averages sometimes show considerable fluctuations not attributable to an effective variation of the light emission from the ground. We assume that this depends on satellite observation limits at night.

The study of the night cloud cover remains in fact an open problem: the satellites are mainly designed for the daytime study and the main weather models, and they may suffer some effects due to cirrus clouds or high aerosol concentration. This is due to the change of the observation band weighting function during the night. The satellite often does not detect low-altitude clouds (Cavazzani et al. 2011; Cavazzani, Ortolani & Zitelli 2012, 2015; Cavazzani & Zitelli 2013). We used the Moderate Resolution Imaging Spectroradiometer (MODIS) to analyse the aerosol optical depth (AOD) and the night cloud cover from 2003 to 2019 in the Veneto region (Italy). The aerosol concentration is another fundamental parameter for site testing (Lombardi et al. 2008). We then made a Fourier analysis of these data by extrapolating the first fundamental periodicity of the two series, and we related them to the lunar synodic cycle

★ E-mail: stefano.cavazzani@unipd.it

[1]https://ngdc.noaa.gov/eog/viirs/download-dnb-composites.html

Table 1. Geographic characteristics of the analysed sites.

Site	Latitude	Longitude	Altitude (m)
Asiago (Ekar Observatory)	45°50′	11°34′	1366
Padua	45°25′	11°53′	12

(Cavazzani, Ortolani & Zitelli 2017; Cavazzani et al. 2019). The presence of the Moon affects the light detection as described in Cavazzani et al. (2020) and Puschnig, Wallner & Posch (2020). The periodicity comparison analyses the various combinations of monthly weather conditions that can generate fluctuations in satellite counts.

In order to quantify the aerosol effects we developed a mathematical model that considers the AOD detected by satellite. We basically adopted the Garstang model for the propagation of light pollution (Garstang 1984, 1986, 1989, 1991, 2007), using the polar satellite data *Suomi National Polar-orbiting Partnership* (*NPP*) and *Aqua*. We also introduced a term for the vehicular traffic contribution and a modified altitude function for the concentration and size of the atmospheric particulate matter.

The light pollution model developed by Kocifaj is also based on the Garstang model (Kocifaj 2007, 2008, 2009). The development of the light pollution models significantly increased in recent years (Aubé et al. 2005, ILLUMINA; Aubé & Kocifaj 2012; Aubé et al. 2014; Aubé & Simoneau 2017, 2018; Simoneau, Aube & Bertolo 2020). In these papers very complex mathematical and physical models are described, which require a high computing capacity and numerous data that are not always available. Our empirical observational model is simpler and it is based on global data. The model could be used for each site to carry out a preliminary analysis and to give important indications for future application of more complex models.

The layout of the paper is as follows. Section 2 illustrates the details of the satellite data products and the Sky Quality Meter (SQM) measurements. In Section 3, we describe the used method to derive information about cloud cover, aerosols, and for analysing VIIRS data. In Sections 4, we describe our mathematical empirical model and provide the physical basis on which it is based. In Sections 5, we apply the model to the Ekar Observatory site and validate it in two particular situations. Finally, in Section 6, we discuss the results and present our conclusions.

2 SATELLITE DATA PRODUCTS AND SQM MEASUREMENTS

In this study, we make use of data provided by the satellites *Aqua*/MODIS and *NPP*/VIIRS. The *Aqua* satellite's orbit has a perigee of 691 km, an apogee of 708 km. *Aqua*/MODIS view the entire surface of the Earth every 1–2 d, acquiring data in 36 spectral bands, or groups of wavelengths. The cloud cover is analysed with the bands 20–36 (see Table 2).

VIIRS is one of five instruments on-board the *Suomi NPP* satellite platform. *Suomi NPP*, previously known as the *National Polar-orbiting Operational Environmental Satellite System Preparatory Project* (*NPP*), is a weather satellite operated by the National Oceanic and Atmospheric Administration (NOAA). The satellite was placed into a Sun-synchronous orbit 824 km above the Earth. The VIIRS instrument observes and collects global satellite observations that span the visible and infrared wavelengths across land, ocean, and atmosphere. The whiskbroom radiometer has 22 channels ranging from 0.41 to 12.01 μm. Five of these channels are high-resolution image bands or I bands, and 16 serve as moderate-resolution bands or M bands. VIIRS also hosts a unique panchromatic day/night band (DNB), which is ultrasensitive in low-light conditions that allows us to observe nighttime lights with better spatial and temporal resolutions compared to previously provided nighttime lights data by the Defense Meteorological Satellite Program (DMSP).

The MODIS data are analysed through GIOVANNI – Interactive Visualization and Analysis website.[2] This tool is designed for visualization and analysis of the atmosphere daily global $1^\circ \times 1^\circ$ products. There is a single image per night. Finally, the VIIRS data provide the mean monthly magnitude in clear sky conditions. The VIIRS sensor is a *Suomi NPP* satellite tool. The imaging DNB provides global data at 742 m spatial resolution and is a calibrated radiometer. The DNB visible bands have a broad spectral range of 0.5–0.9 μm centred at 0.7 μm and they have ability to collect low-light imagery at night[3] (Cao et al. 2017).

The ground sky brightness measurements were carried out in both sites with a Sky Quality Meter-Lens Ethernet (SQM-LE) pointed to the zenith. The SQM-LE measures the brightness of the night sky every 5 min through an Ethernet connection, while the temperature sensor compensates the readings for various operating temperatures. SQM has a spectral range between 350 and 700 nm, with its peak between 500 and 550 nm. The SQM is one of the main tools for the light pollution analysis. The main features are described in Cinzano (2005, 2007). The ALAN study was further developed and linked to the new SQM networks in Bará (2016), Bará, Lima & Zamorano (2019), and Ribas et al. (2016). SQM networks are widely used, as described in Bertolo et al. (2019), Espey & McCauley (2014), Posch, Binder & Puschnig (2018), and Pun & So (2012). Other tools are described in Hanel et al. (2017).

3 METHODS AND DATA ANALYSIS

We use three groups of satellite time series: nightly cloud fraction (MODIS), nightly AOD (MODIS), and nightly SQM ground data. The nightly cloud fraction is defined as the number of cloudy pixels divided by the total number of pixels. Satellite data also provide the amount of sky estimated to be covered by a specific cloud type (cirrus, contrail, cirrostratus, cumulus, etc.), cloud particle phase (water, ice, liquid, mixed), cloud height (low, middle, high), or by all cloud types (total cloud fraction). Cloud differs from fog only in that the latter is, by definition, close (a few metres) to the ground. Aerosol optical depth is the degree to which aerosols prevent the transmission of light by absorption or scattering of light. The AOD is defined as the integrated extinction coefficient over a vertical column of unit cross-section. Extinction coefficient is the fractional depletion of radiance per unit pathlength. AOD is available through GIOVANNI at 550 nm from the MODIS. We analyse the nightly available data from 2003 to 2019 (about 3200 values) at the Veneto region from *Aqua* satellite. In this paper, the MODIS data and the respective thresholds are processed and provided by GIOVANNI – Interactive Visualization and Analysis website. The third time series is the VIIRS data, this is provided in monthly averages. Finally, to validate the model we use the SQM high temporal resolution network of the Veneto region (Bertolo et al. 2019). In particular, we analyse the nightly data from 2012 to 2019 sampled every 5 min at Ekar Observatory. The idea of

[2] https://giovanni.gsfc.nasa.gov

[3] https://ncc.nesdis.noaa.gov/documents/documentation/viirs-users-guide-tech-report-142a-v1.3.pdf

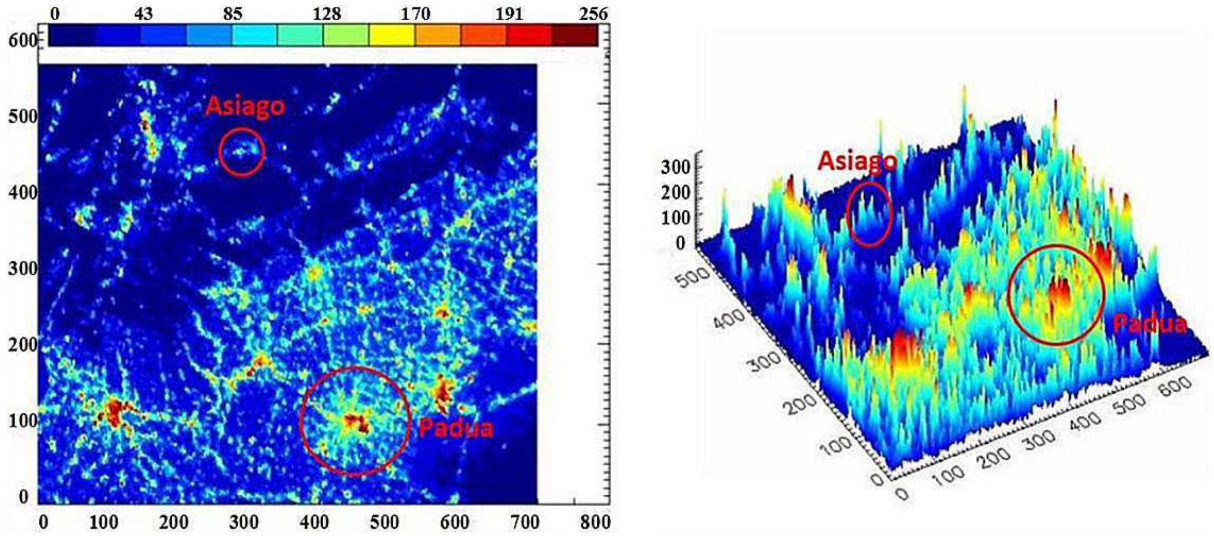

Figure 1. Location of the analysed site. Interactive Data Language (IDL) two-dimensional reconstruction (left-hand panel) and three-dimensional reconstruction (right-hand panel) of the light emission from the ground at Veneto region (Italy) in 2019 January. The image is a matrix of 700 × 550 pixels corresponding to 140 × 110 km, the colours of the bar above the left-hand panel define the satellite counts processed with IDL.

Table 2. MODIS bands. The spatial resolution of the bands is 1 km.

Primary use	Band	Bandwidth (μm)
Surface/cloud temperature		
	20	3.660–3.840
	21	3.929–3.989
	22	3.929–3.989
	23	4.020–4.080
Atmospheric temperature		
	24	4.433–4.498
	25	4.482–4.549
Cirrus clouds water vapour		
	26	1.360–1.390
	27	6.535–6.895
	28	7.175–7.475
Cloud properties		
	29	8.400–8.700
Ozone		
	30	9.580–9.880
Surface/cloud temperature		
	31	10.780–11.280
	32	11.770–12.270
Cloud top altitude		
	33	13.185–13.485
	34	13.485–13.785
	35	13.785–14.085
	36	14.085–14.385

correlating the main periods of cloud cover and aerosols with lunar cycles arises from the visual analysis of the nightly data of the *NPP* satellite.[4] Fig. 2 shows VIIRS data 2D (top left-hand panel) and 3D (top central panel) reconstructions of a clear night with a new Moon (2020 April 23) compared to a 3D reconstruction of a cloudy night in the new Moon period (2020 April 26, 8 per cent visible Moon, top right-hand panel). 2D (bottom left-hand panel) and 3D (bottom central panel) reconstructions of a clear night in the full Moon period (2020 May 5, 91 per cent visible Moon) can be compared to the 3D reconstruction of a cloudy full Moon night (2020 May 6, 97 per cent visible Moon, bottom right-hand panel). The scale is the same as Fig. 1 (700 × 550 pixels corresponding to 140 × 110 km). We can see how satellite measurement is highly influenced by the presence of the Moon. The problem of nighttime cloud cover from the satellite is still open (Cavazzani et al. 2015). In some cases the satellite does not detect some types of night clouds and, as some fluctuations indicate, does not consider the concentration of aerosols. However, this effect must be related to the lunar cycles because it influences the satellite measurement in two ways: clear skies, high aerosol concentration, and full Moon period, higher counts; clear skies, high aerosol concentration, and new Moon period, lower counts. We show afterwards that this does not happen with SQM ground measurements at an ALAN contaminated site.

The role of aerosols is also described in Kocifaj & Kómar (2016), Horvath (2014), and Bohren & Huffman (1998). These important works also used for the development of the Section 4.

The high concentration of aerosols induces an increase in the radiance values. This can be explained visually through the Fig. 3 that is a schematic representation of the empirical observation model. This figure shows an observatory (O), a generic source city (S), and a generic point (P) in the sky. A high concentration of aerosols (red layer) leads to an increase of single scattering and multiple scattering (MS) on SQM ground measurements. Satellite data are mostly influenced by the Moon, which produces a double effect. A high concentration of aerosols in the full Moon period causes an increase in satellite counts, while a high aerosol concentration in the new Moon period causes a decrease in satellite counts. We use Fourier analysis to extrapolate the main cloud cover and aerosol periodicities and correlate them with the synod lunar month.

3.1 Fourier analysis: fast Fourier transform

The Fourier analysis consists in the possibility of representing complicated periodic structures using combinations of simple periodic

[4] https://maps.ngdc.noaa.gov/

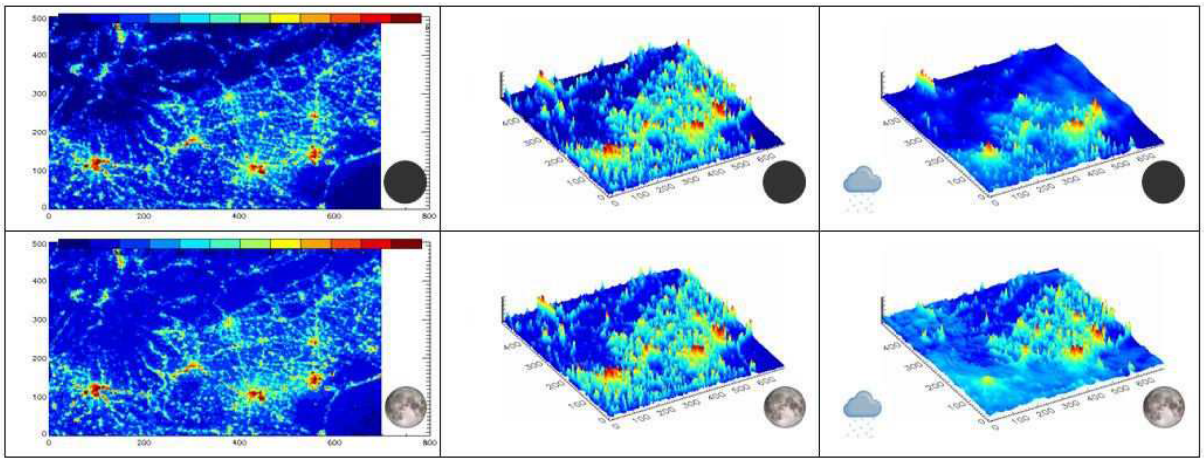

Figure 2. VIIRS data 2D (top left-hand panel) and 3D (top central panel) reconstructions of a clear night with a new Moon (2020 April 23) compared to a 3D reconstruction of a cloudy night in the new Moon period (2020 April 26, 8 per cent visible Moon, top right-hand panel). 2D (bottom left-hand panel) and 3D (bottom central panel) reconstructions of a clear night in the full Moon period (2020 May 5, 91 per cent visible Moon) compared to the 3D reconstruction of a cloudy full Moon night (2020 May 6, 97 per cent visible Moon, bottom right-hand panel).

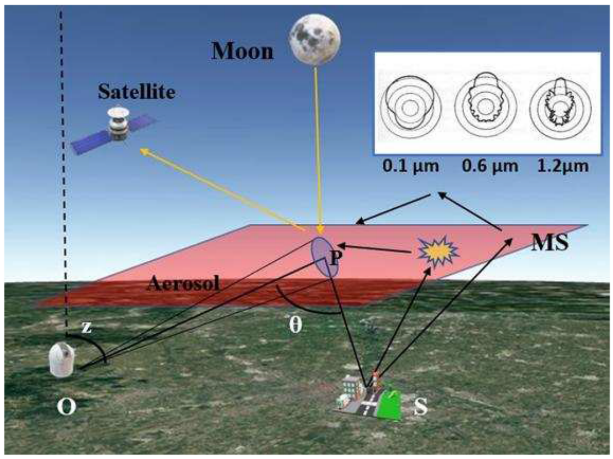

Figure 3. Schematic representation of the empirical observation model as a function of the zenith angle z. Figure shows an observatory (O) and a generic source city (S) under an angle θ referred to a point (P). A high concentration of aerosols leads to an increase of single scattering and multiple scattering (MS). The satellite data analysis and the comparison with the ground data involve the inversion of the frontscatter with the backscatter. A high concentration of aerosols in the full moon period causes a strong satellite frontscatter. The top right-hand panel shows the scattering as a function of the particle size: particles of smaller diameter increase the scattering and its dispersion.

functions. A function can be described by its value $f(t)$ or its amplitude $F(\omega)$ of the frequency ω. The Fourier transform (FT) converts $f(t)$ in $F(\omega)$ and vice versa, the FT allows switching between the time domain to the frequency of a physical phenomenon.

Since the data are discrete in applications we use the discrete Fourier transform (DFT), which transforms a real or complex vector in another whose components are a combination of periodic functions. The DFT is the equivalent of the continuous FT for signals known only at N instants separated by sample times T (i.e. a finite sequence of data):

$$F(\omega) = \int_{-\infty}^{+\infty} f(t)\, \mathrm{e}^{-j\omega t}\, \mathrm{d}t, \tag{1}$$

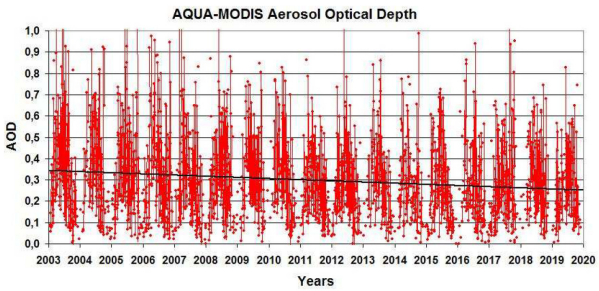

Figure 4. Nightly trend of the aerosol optical depth over the Veneto region (Italy) from 2003 to 2019. Figure shows the annual periodicity of the aerosol concentration, while the long-term trend shows a decrease given by the linear regression of equation $y = 5.5 \times 10^{-3}x + 0.34$ and a mean total value of 0.30.

$$F(\omega) = \sum_{k=0}^{N-1} f[k]\, \mathrm{e}^{-j\omega kT}, \tag{2}$$

with N data number and $k = 0, 1, 2,..., N - 1$.

3.1.1 *The Cooley–Tukey algorithm*

The fast Fourier transform (FFT) is an algorithm for the fast calculation of the DFT. FFT is usually applied extending the original N-long record to an N'-long record such that $N' = 2^n$ for a given n. The extension is done with zeroes after having removed the average from the original record. The strategy underlying the FFT algorithms is to bring the calculation of a DFT of length N to the calculation of lower length DFT. In particular, in the radix-2 FFT algorithms, a DFT of length $N = 2^n$ is reduced to the calculation of length 2 DFT (Cooley & Tukey 1965).

We have applied the FFT to the cloud cover and aerosols data at Veneto region (2003–2019) presented in Fig. 4. The AOD nightly time series presents a strong seasonal cyclicity, a mean total value of 0.30 and furthermore the linear regression highlights a long-term decrease given by the equation

$$y = -5.5 \times 10^{-3}x + 0.34. \tag{3}$$

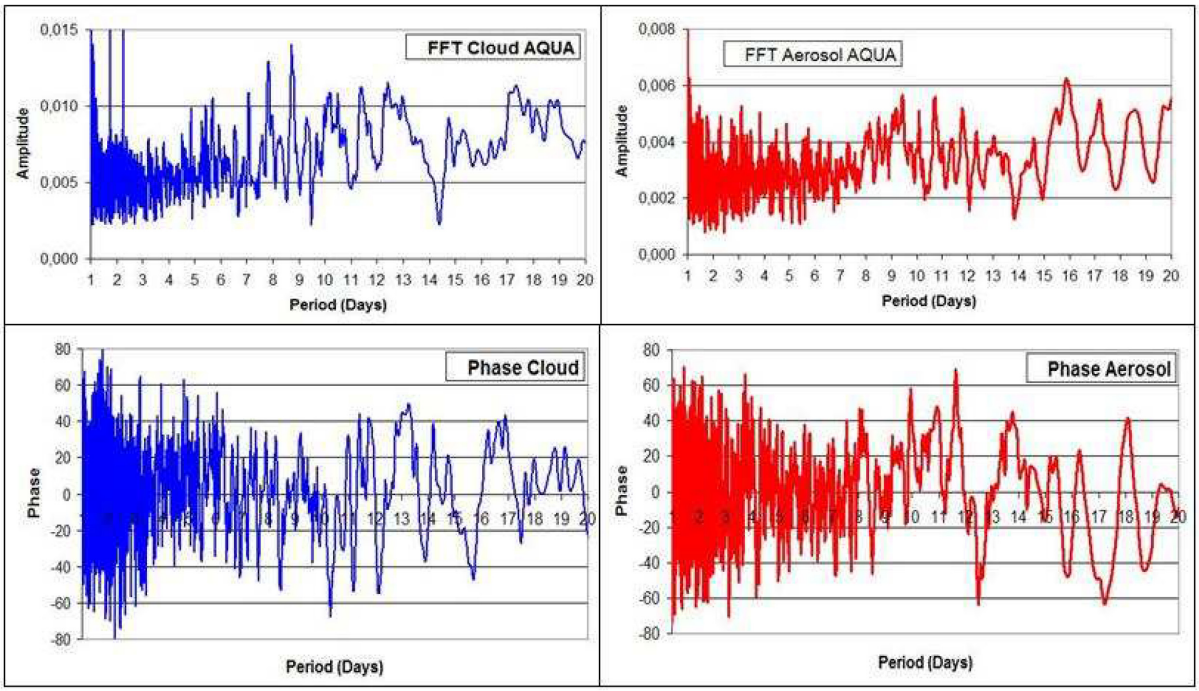

Figure 5. FFT of the night cloud cover (top left-hand panel) over the Veneto region (Italy) from 2003 to 2014 with the respective phase associated with each periodicity (bottom left-hand panel) and the FFT of the aerosol optical depth (top right-hand panel) over the Veneto region (Italy) from 2003 to 2014 with the respective phase associated with each periodicity (bottom right-hand panel).

Fig. 5 shows the FFT trend, after the conversion of the main frequencies in main periods, top right-hand panel and top left-hand panel for cloud cover and aerosols, respectively. The error analysis on the period of this peak is provided in three independent different ways allowing a triple check of the validity of the obtained results. The first analysis is based on the error propagation and provides the maximum error due to the sampling of the data. Through the propagation formula described in Cavazzani et al. (2017) we reach the total maximum error of 5 per cent, which corresponds to an uncertainty of ±10 h for the 8.7 d cloud cover peak and ±19 h for the 16 d aerosols peak. The second error is based on the frequency resolution of the Fourier analysis defined as

$$\nabla f = \frac{1}{T} = \frac{f_{\rm P}}{N},$$

where T is the period, $f_{\rm P}$ is the frequency of the peak, and N is the number of analysed data during the period. A frequency $f_{\rm P}$ associated with a spectral peak has an uncertainty of $\pm\frac{1}{2}\nabla f$ and the correspondent period P is

$$P = \frac{1}{f \mp \frac{1}{2}\nabla f} = \frac{1}{f} \pm \frac{\nabla f}{2f^2} = \frac{1}{f} \pm \frac{P^2}{2T}. \quad (4)$$

From this formula we get an uncertainty of ±1 h for the 8.7 d cloud cover peak and ±1 h for the 16 d aerosols peak. Finally, if we compare this result with the full width at half-maximum (FWHM) of the analysed peak, we can verify the validity of our analysis. Fig. 5 shows the obtained results: the top left-hand panel reproduces the trend of the FFT night cloud cover over the Veneto region (Italy) from 2003 to 2019 with the respective phase associated with each periodicity (bottom left-hand panel). The top right-hand panel reproduces the trend of the FFT aerosol optical depth over the Veneto region (Italy) from 2003 to 2019 with the respective phase associated with each periodicity (bottom right-hand panel). We can see how the cloud cover FFT shows two comparable peaks at 8.0 and 8.7 d. We have chosen the one of greater amplitude, while the 16.0-d peak of the AOD appears better defined. The respective phases of +20° on an 8.7-d peak corresponding to +12 h and of −20° on a 16-d peak corresponding to −21 h correlate the two time series with the lunar synodic month as shown in Fig. 6. Synodic lunar months (M) are compared to the simulation of the main cloud cover (C) and AOD (A) periodicities obtained from Fourier analysis. The main periodicities and phases refer to 2019 January. Fig. 6 shows 4 months with combinations of different atmospheric conditions: January with the full Moon in conjunction with a cloud cover and AOD peak; February with the full Moon combined with a clear sky and an AOD peak; March with the full Moon period without aerosols in clear sky conditions; and April with clear sky conditions during the new Moon in the presence of AOD peak. Fig. 7 shows the empirical validation of the model: triple comparison between the satellite values of cloud cover, aerosols, and lunar cycles of the first four months in 2019 at the Veneto region (top panel). Fig. 7 analyses four different conditions: January with full Moon in cloudy conditions (VIIRS radiance, central left-hand panel); February with full Moon in clear conditions and high aerosol concentration (VIIRS radiance, central right-hand panel); March with full Moon in clear conditions and low aerosol concentration (VIIRS radiance, bottom left-hand panel); and April with the period close to the new Moon in clear conditions and high aerosol concentration(VIIRS radiance, bottom right-hand panel). The four images are matrices of 120 × 80 pixels corresponding to 24 × 16 km. January and March are the most reliable satellite measurements, since in January the satellite excludes the nights covered in the full Moon period, while in March the clear full Moon period has a low AOD. The greater radiance detected by satellite in January is probably due to the Christmas lighting devices that are removed in February. The critical months in which we see the dual effect of aerosols on satellite measurements are February and April:

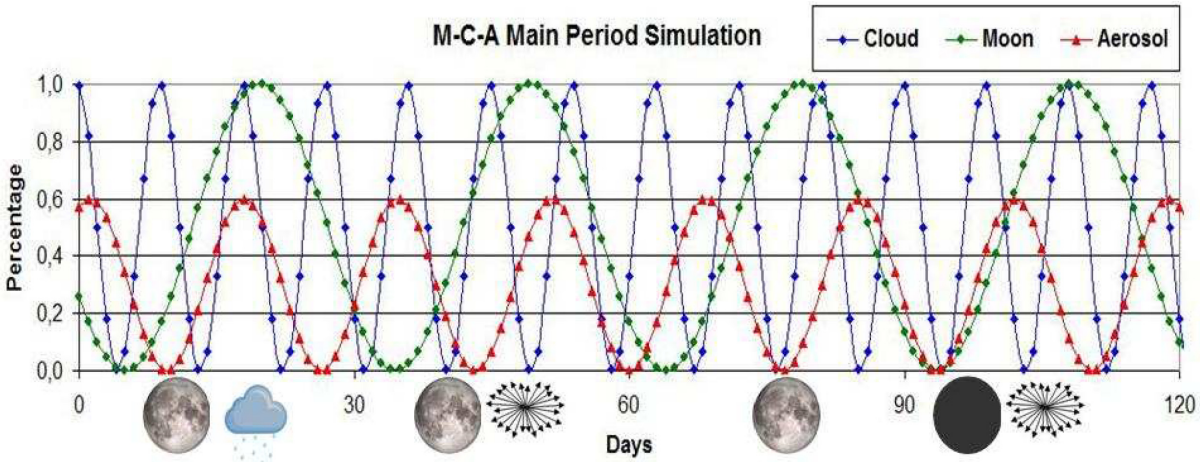

Figure 6. Synodic lunar month (M) compared with the simulation of the main cloud cover (C) and AOD (A) periodicities obtained from Fourier analysis. The main periodicities and phases refer to 2019 January. Figure shows 4 months with combinations of different atmospheric conditions: January with the full Moon in conjunction with a cloud cover and AOD peak; February with the full Moon combined with a clear sky and an AOD peak; March with the full Moon period without aerosols in clear sky conditions; and April with clear sky conditions during the new Moon in the presence of AOD peak.

in February we have the clear full Moon period with high AOD that causes an increase in radiance detected by satellite because aerosols diffuse and reflect lunar light radiation. In April, we have the clear new Moon period with high AOD that causes a decrease in radiance detected by satellite because the aerosols block the light radiation from the ground. This is the first important result of our paper. These fluctuations are photometrically analysed in Fig. 8 where the light emission of the Asiago municipality detected by satellite for the first four months in 2019 is shown. The top left-hand panel reproduces the satellite count trend as a function of the radius from the city centre in January, the top right-hand panel for February, the bottom left-hand panel for March, and the bottom right-hand panel for April. This figure shows the largest satellite measurement fluctuations in the maximum count and in the area included in $5 < r < 10$ pixels, where 5 pixels correspond to 1 km.

3.2 Data analysis: conversion technique

In this section, we describe the calculation for the radiance measurement detected by satellite. There are numerous papers describing the various conversion models for elaborating detailed light pollution atlases (Cinzano, Falchi & Elvidge 2001; Falchi et al. 2016). In this work, we use a different approach: we do not need an absolute calibration for the analysis of fluctuations, but we directly analyse the satellite data. The calculation of the radiance measured by satellite is carried out through a volume integral of the ground light emission (see Fig. 9). We locate on the plane (longitude–latitude) a boundary field Π where we define a continuous function:

$$z = f(x, y).$$

The field Π is contained in a rectangle that defines two pairs of functions:

$$\mathrm{DAC} \Rightarrow x = \varphi_1(y),$$

$$\mathrm{CBD} \Rightarrow x = \varphi_2(y).$$

The second couple:

$$\mathrm{ADB} \Rightarrow y = \phi_1(x),$$

$$\mathrm{ACB} \Rightarrow y = \phi_2(x).$$

The volume of the solid bounded by the field Π and the surface $z = f(x, y)$ is given by the formula of subsequent integrations:

$$V = \int_{\phi_1(x)}^{\phi_2(x)} \mathrm{d}y \int_{\varphi_1(y)}^{\varphi_2(y)} f(x, y)\,\mathrm{d}x. \tag{5}$$

The volume value is used for the calculation of radiance expressed in $\left[\frac{nW}{m^2\,sr}\right]$.

4 EMPIRICAL MATHEMATICAL MODEL OF ALAN PROPAGATION

In this section, we describe a mathematical model that considers the influence of AOD on NSB according to the empirical evidence found in Section 3. This model, based on the Garstang model, uses the AOD satellite data. We also introduced a term for the vehicular traffic contribution (T) and a modified altitude function for the concentration ($n(h)$) and size ($s(h)$) of the atmospheric particulate matter.

We now introduce the physical bases on which our model is based. The light scattered in the sky is partially diffused by the particles of the Earth's atmosphere producing the sky luminescence causing light pollution. The low atmosphere is formed of gases whose concentration remains constant with altitude and that are nitrogen, oxygen, and argon. Other gases have a variable concentration: water vapour (H_2O), carbon dioxide (CO_2), anhydride sulphurous (SO_2), and ozone (O_3). The concentration of water vapour varies in relation to its evaporation–condensation–precipitation cycle that takes place within the first 12–14 km of atmosphere. Aerosols are liquid, solid, or mixed particles suspended in the atmosphere. They are present in concentrations variable with respect to place and time. Their concentration decreases with altitude and distance from the most densely populated regions. Aerosols are also part of the condensation process of water vapour that occurs when the air that contains them, saturated with water vapour, undergoes a sharp drop in temperature. Some weather conditions can favour an accumulation of gas and aerosols due to pollution, such as the presence of anticyclones that make the air layer at ground level stable, promoting the stagnation of the air at night. We can simplify the atmospheric structure considering it a gas in equilibrium with the gravitational attraction:

$$\mathrm{d}p = -g\rho\,\mathrm{d}h, \tag{6}$$

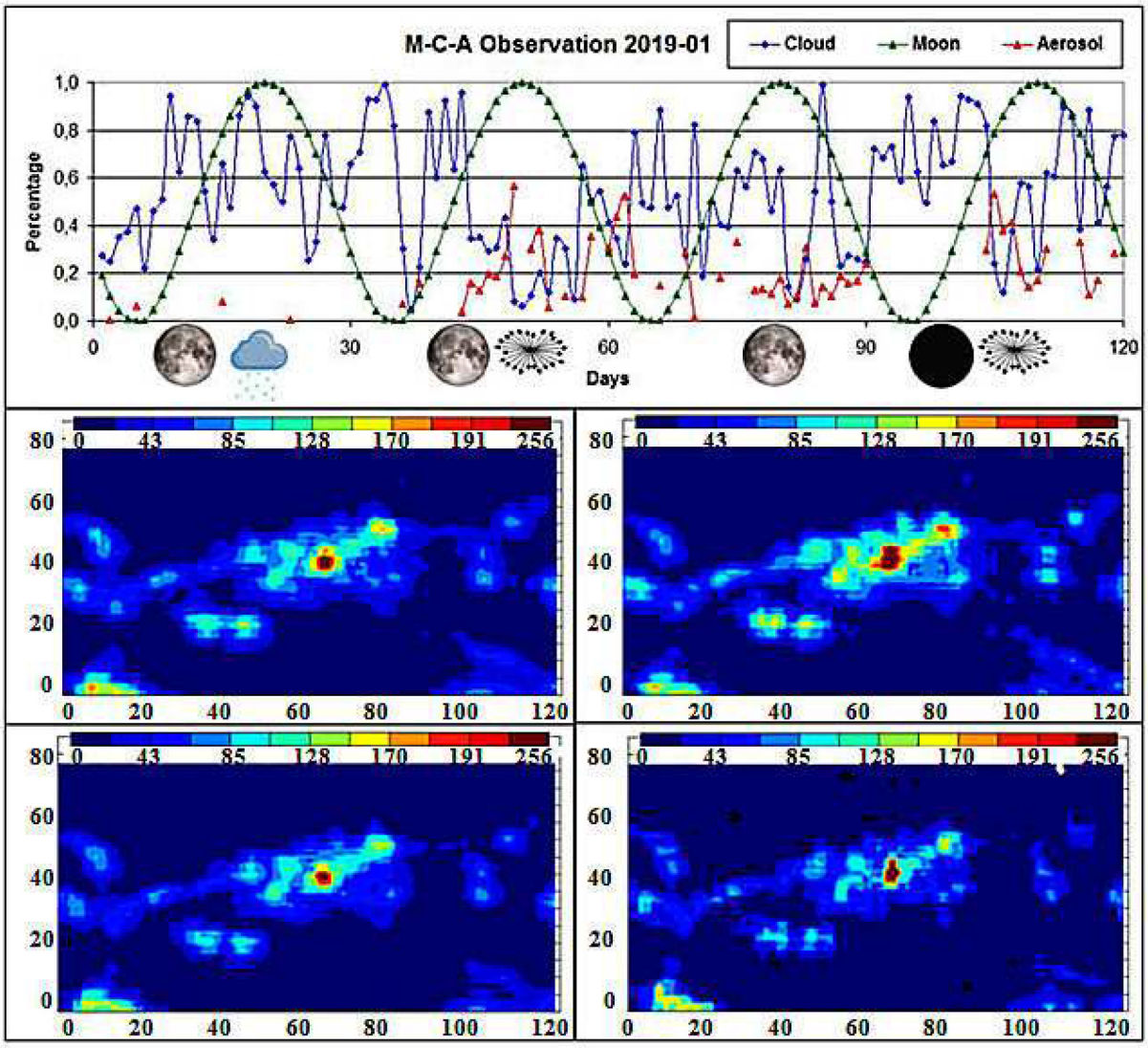

Figure 7. Triple comparison between the satellite values of cloud cover, aerosols, and lunar cycles of the first four months in 2019 at the Veneto region (top panel). Figure shows four different conditions: January with full Moon in cloudy conditions (VIIRS radiance, cental left-hand panel); February with full Moon in clear conditions and high aerosol concentration (VIIRS radiance, cental right-hand panel); March with full Moon in clear conditions and low aerosol concentration (VIIRS radiance, bottom left-hand panel); and April with the period close to the new Moon in clear conditions and high aerosol concentration (VIIRS radiance, bottom right-hand panel). The four images are matrices of 120 × 80 pixels corresponding to 24 × 16 km.

the state equation of a perfect gas is valid considering dry air:

$$P = \rho \frac{RT}{M},$$

where M is the mass of a mole of dry air. Obtaining the density from the last equation, replacing it in equation (6) and integrating with T, g, and M we find that the density of the atmospheric gaseous component decreases exponentially with altitude:

$$P = P_0 \, \mathrm{e}^{-\frac{Mg}{RT}h}$$

and

$$\rho = \rho_0 \, \mathrm{e}^{-\frac{Mg}{RT}h}.$$

Also the density of aerosols in general decreases exponentially with altitude. The effects on light propagation of the molecules and aerosols are scattering and absorption phenomena. Both reduce the energy of a light beam causing extinction.

4.1 Rayleigh and Mie scattering

We first consider small particles compared with the wavelength of visible light: the molecules and the smallest aerosol particles. In this case the particle can be considered immersed in a periodic homogeneous electric field that polarizes it by inducing a dipole moment,

$$\boldsymbol{p} = \bar{\alpha} \boldsymbol{E}_0 \, \mathrm{e}^{\mathrm{i}\omega t},$$

where $\bar{\alpha}$ is the proportionality constant called polarization tensor. The dipole oscillating radiates electromagnetic waves in all directions generating the Rayleigh scattering (RS). The radiation intensity due to RS in a given direction as a function of the incident beam intensity and direction for an isotropic medium is

$$I = \frac{I_0}{r^2}(1 + \cos^2\theta)\frac{|\alpha|}{2\lambda^4},$$

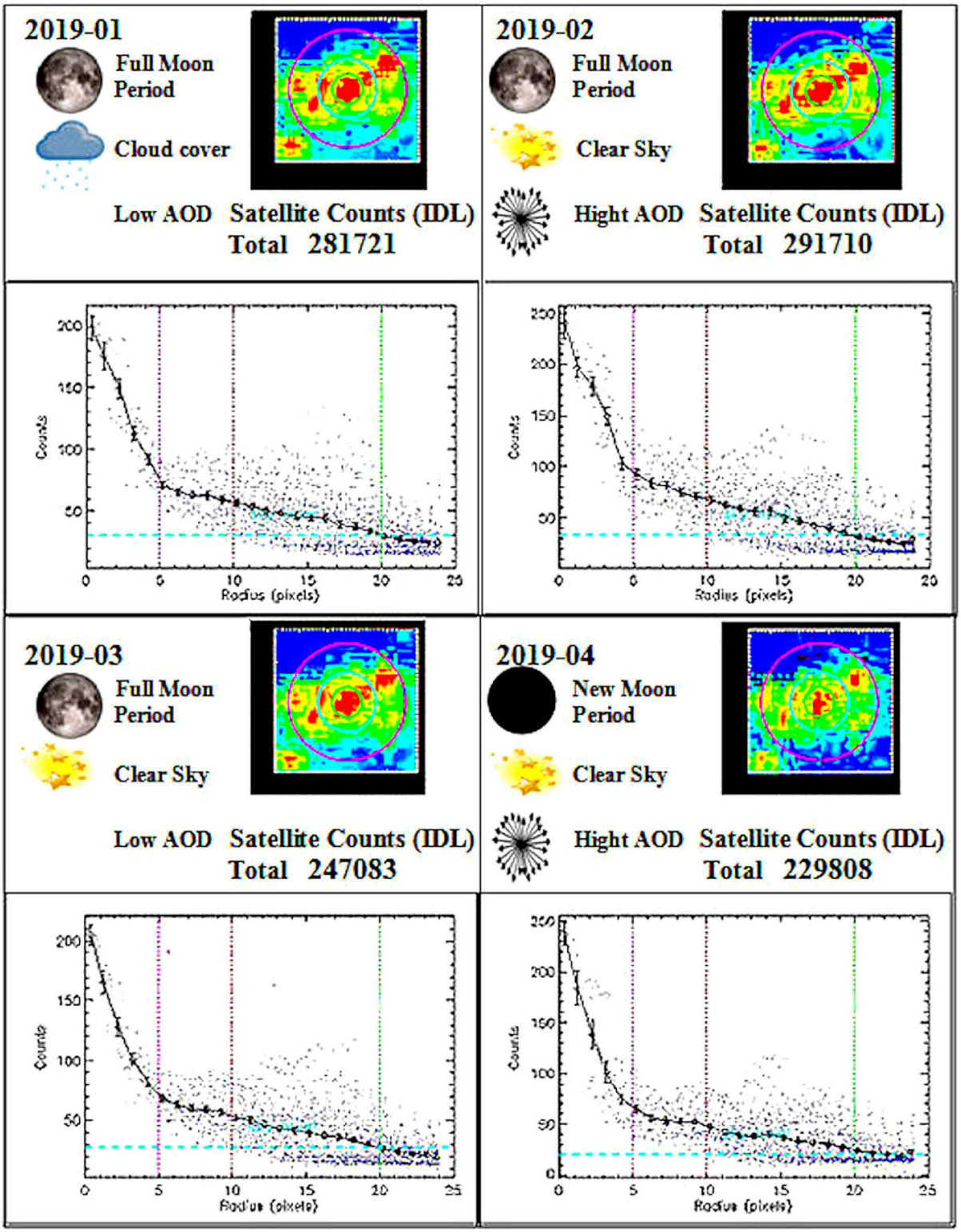

Figure 8. Photometric analysis of the light emission of the Asiago municipality detected by satellite for the first four months in 2019. The top left-hand panel shows the month of January, the top right-hand panel for February, the bottom left-hand panel for March, and the bottom right-hand panel for April. Figure shows the largest satellite measurement fluctuations in the maximum count and in the area included in $5 < r < 10$, where 5 pixels correspond to 1 km.

where $|\alpha|$ is the scalar polarizability. The light diffusion in the case of particles with dimensions comparable or greater to the wavelength of visible light (aerosols) is due to refraction and reflection. The angular distribution, the light polarization, and the energy absorbed depend on the shape, the composition, the refractive index, and the surface characteristics of the particles. For a spherical particle the radiation diffused by refraction is concentrated in a direction close to that in which the incident radiation propagates (frontscatter). Another cause

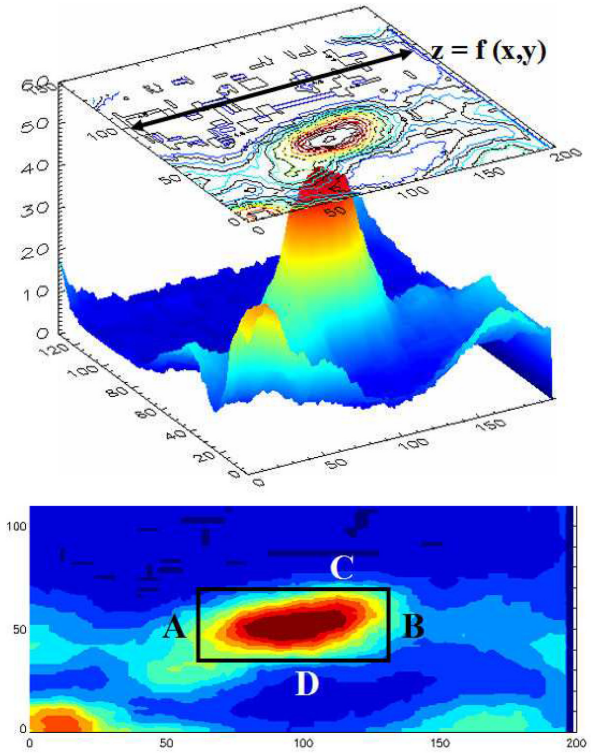

Figure 9. The volume value is used for the calculation of radiance.

of light diffusion is the reflection from the surface of the particles. Reflection can be distinguished in specular reflection or widespread reflection. Let us examine, for example, the behaviour of light on the surface of a spherical particle. The intensity of the diffused radiation by a spherical particle that completely re-emits the incident light has the following expression (Schoenberg 1929):

$$f(\theta) \propto \sin\theta - \theta\cos\theta,$$

it is maximum for the opposite direction of the incident rays (backscatter). Real particles generally have a reflective part and a diffusing part surface. We can now define a diffusion function using Mie's theory (Mie 1908) of the radiation diffusion:

$$f(\theta) = \frac{\phi(\theta)}{\phi_{\rm Incident}}.$$

4.2 ALAN propagation model

The total light emitted in the sky is

$$L = \sum_k \phi_k \left[\epsilon_k + (1-\epsilon_k)\eta_k + (1-\epsilon_k-(1-\epsilon_k)\eta_k)j_k\right],$$

where ϕ_k is the total flow emitted by the k-light point, ϵ_k is the fraction of light scattered directly above the horizon, η_k is the diffusion fraction light, and j_k the fraction of light reflected in the sky from the illuminated area. The diffusion from the particles of the atmosphere grows exponentially with the optical path travelled. The quantity of diffused light dI in a path dh is

$$\mathrm{d}I = -IN\sigma\,\mathrm{d}h,$$

where $N = \frac{N_{\rm Particles}}{\rm Volume}$ and σ is the integrated cross-section. The fraction of scattered light along a path d is

$$\eta = 1 - \mathrm{e}^{-N\sigma d}.$$

We assume that the light from a city is uniformly spread. Then the emission of this ideal total surface follows Lambert's law, i.e. its brightness B is constant in all directions. In this approximation the intensity re-emitted upwards is

$$I_{\rm R} = \frac{\phi(1-\epsilon)(1-\eta)j}{\pi}\cos\theta.$$

The light coming directly from the source is

$$I = I_0\,\mathrm{e}^{-\sigma Nd} = I_0\,\mathrm{e}^{-\tau},$$

where

$$\tau = (N_{\rm Mol}\sigma_{\rm Mol} + N_{\rm Aer}\sigma_{\rm Aer})d.$$

In a realistic atmospheric model the numerical density of $N_{\rm Mol}$ molecules and $N_{\rm Aer}$ aerosols depend on the altitude h:

$$\tau = \int_0^{h_{\rm Max}} (N_{\rm Mol}(h)\sigma_{\rm Mol} + N_{\rm Aer}(h)\sigma_{\rm Aer})\sec z\,\mathrm{d}h. \quad (7)$$

We approximate the vertical distribution of aerosols and molecules with two exponential functions having radii of scale $r_{\rm Mol}$ and $r_{\rm Aer}$, respectively, obtaining from the integration of the equation (7):

$$I = I_0\exp[N_{0,\rm Mol}\sigma_{\rm Mol}(1-\mathrm{e}^{h_{\rm Max}/r_{\rm Mol}})r_{\rm Mol} + N_{0,\rm Aer}\sigma_{\rm Aer}(1-\mathrm{e}^{h_{\rm Max}/r_{\rm Aer}})r_{\rm Aer}]\sec z. \quad (8)$$

We obtain the flow per unit of surface ζ (illuminance) at point P produced by the light coming directly from the source S:

$$\zeta = \frac{I_0}{d^2}\,\mathrm{e}^{-\tau}. \quad (9)$$

We make a simple estimate of the scattering effect following the method suggested by Treanor (1973). We call S the source city, P the particle located along the line of sight that sends part of the incident light to the observer O (see Fig. 3). The flow per unit area in P is

$$\zeta = \int_S^P \left[\frac{I_{\rm S}}{x^2}\,\mathrm{e}^{-kx}\right]\sigma N\epsilon\left[\frac{\mathrm{e}^{-k(d-x)}}{(d-x)^2}\right]\mathrm{d}x, \quad (10)$$

where

$$\epsilon = \pi\theta^2\frac{x^2(d-x)^2}{d^2},$$

which inserted in equation (10) and integrated provides (Treanor 1973)

$$\zeta = \sigma N\pi\theta^2 I_{\rm S}\frac{\mathrm{e}^{-kd}}{d}.$$

We assume that the molecules diffuse the incident light by Rayleigh scattering and the aerosols by Mie scattering. This assumption is functional and effective for the aims of this paper although not generally applicable. θ is the SPO angle. The angular cross-section of the Rayleigh scattering and the Mie scattering are

$$\sigma_{\rm Mol}(\theta) = \sigma_{0,\rm Mol}\frac{3}{16\pi}(1+\cos^2\theta) \quad (11)$$

and

$$\sigma_{\rm Aer}(\theta) = \sigma_{\rm Aer}\,f(\theta). \quad (12)$$

The flow received by O in a unitary area from an angular area of sky ω is

$$\phi = \int\left(E_{\rm SP}\frac{I_{\rm S}}{s^2} + \zeta_{\rm ms}\right)\frac{1}{u^2}E_{\rm PO} \times [N_{\rm Mol}(h)\sigma_{\rm Mol}(\theta) + N_{\rm Aer}(h)\sigma_{\rm Aer}(\theta)]\,\omega u^2\,\mathrm{d}u, \quad (13)$$

where E_{SP} and E_{PO} are the extinctions along the SP and PO lines, respectively (see Fig. 3). ζ_{ms} is the multiple scattering flow per unit of surface in the hypothesis of the Extended Garstang Model (EGM; Cinzano & Falchi 2012). The multiple scattering mechanisms are also treated analytically for all scattering orders in Kocifaj (2018), but the approximations of the EGM are still accurate in this application. The sky brightness due to light pollution is given by the flow per unit of solid angle:

$$b = \frac{\phi}{\omega}.$$

The sky brightness in magnitudes is obtained from the sum of artificial and natural sky brightness:

$$m = \text{constant} - 2.5 \log(b_{\text{Nat}} + b_{\text{Art}}). \tag{14}$$

Our model, according to the theoretical bases just explained, is described by the following formula:

$$I = P \times T \times D^{-a} \times MS^{-b} \times E, \tag{15}$$

where P is the population, D is the distance, a and b are constants in the range $-2.4 < a < -1.8$ and $0.8 < b < 1.2$, respectively, dependent on empirical calibration of the analysed site. T (traffic contribution) is

$$T = A\, \mathrm{e}^{-\frac{\Delta t}{\Delta t_N}} P \sum_{\text{headlight}} [\epsilon + (1-\epsilon)(\eta + (1-\eta) j)]\,. \tag{16}$$

The constant A depends on the nation and city analysed and it is in the range $0 < A < 1$. Δt is the time interval in which the traffic contribution is calculated and Δt_N the duration of the night.

The multiple scattering factor (MS) is

$$\text{MS} = \frac{N_{\text{Mol}}(\theta) n(h) \sigma_{\text{Mol}}(\theta) s(h)}{\cos^c(\theta)} + \frac{\text{AOD}_{\text{Sat}} n(h) \sigma_{\text{Aer}}(\theta) s(h)}{\cos^d(\theta)}, \tag{17}$$

where c and d are empirical constants in the range $0.8 < c < 1.2$ and $0.5 < d < 1.5$, respectively, depending on empirical calibration of the analysed site, and $n(h)$ and $s(h)$ are

$$n(h) = \left[\mathrm{e}^{-\text{const} \times h}\right] \int_{h_O}^{h_S} N \, \mathrm{d}h \tag{18}$$

and

$$s(h) = \left[\mathrm{e}^{-\text{const}_1 \times h}\right] \int_{h_O}^{h_S} \sigma \, \mathrm{d}h. \tag{19}$$

Finally, we define the extinction factor (E):

$$E = \text{const} \times \left[\frac{2\pi\sigma(h)}{\lambda}\right]^f, \tag{20}$$

where f is empirical constant in the range $0.5 < c < 1.5$. All constants are empirically calculated through the correlation with SQM ground data and the VIIRS satellite data. Fig. 10 represents six model simulations by varying the AOD_{Sat} and the mean particle radius. We consider a low AOD_{Sat} of 0.2 and a high AOD_{Sat} of 0.5 associated with three mean radii of 1.2, 0.6, and 0.1 μm as a function of the zenith angle. The smaller particles scattering more light as shown in the top right-hand panel of Fig. 3.

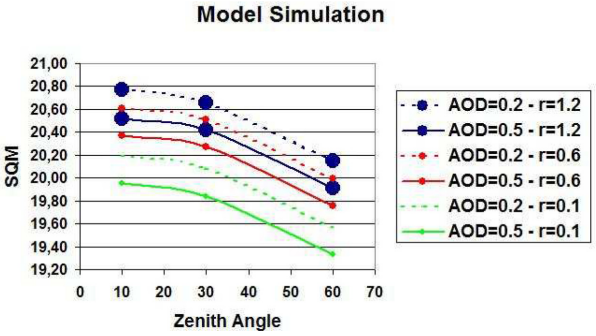

Figure 10. Model simulation as a function of the zenith angle, concentration, and size of the aerosols at the Ekar Observatory. We consider an observation wavelength of 500 nm.

5 LIGHT POLLUTION AT EKAR OBSERVATORY IN ASIAGO

Asiago is a site contaminated by ALAN (see Fig. 1) and has cloud cover conditions around 40 per cent per year. The total observation time, including mixed nights, is about 60 per cent per year.[5] Finally, it does not have stable nighttime conditions, therefore the low temporal and spatial resolution of the *Aqua* satellite does not provide results in terms of observation time but in terms of photometric night. We applied the model described above to the Ekar Observatory considering the main neighbouring cities. Table 3 provides the results of the analysis: in column 1 we see the city, in column 2 the population (N), in column 3 the traffic contribution (number of vehicles N_1). We requested at the local administration for the data of the Padua city. The data show that at sunset the average value of the vehicles entering and leaving the city is around 94 000, corresponding to 45 per cent of the population ($A = 0.45$ in equation 16). Traffic data were provided to us every 5 min from 20:00 to 05:00 (Δt and Δt_N in equation 16). The model provides a number of vehicles at 01:00 of 16 000 vehicles against the 15 500 provided by the municipal police. We use the same A value for the Veneto region, even if for the plateau towns (Asiago and Gallio) this value could be lower. However, the traffic in these towns has a low influence on the model due to the low population. In column 4 the distance from the Ekar Observatory (D), in columns 5 and 6 the altitude and the difference in altitude (h and Δh) compared to the observatory used in equations (18) and (19). We suppose an $\text{AOD}_{\text{Sat}} = 0.2$, an aerosol mean radius of 1.2 μm to use in equation (17), a zenith angle of 5°, and the observation wavelength $\lambda = 500$ nm. In column 7 the radiance contribution of each city to the Ekar Observatory site and in column 8 we provide the contribution percentage of each source. The last line of the table gives the NSB model result for the Ekar Observatory converted to ($\left[\frac{\text{mag}}{\text{arcsec}^2}\right]$). We note that the percentage due to the Asiago plateau is 36.7 per cent (Gallio plus Asiago), while the Po Valley influences for the rest 63.3 per cent. The validation of these results is done through the analysis of two peculiar situations. Fig. 11 shows two nights measured by VIIRS: the top left- and right-hand panels are the 2D and 3D reconstructions of a clear night (2020 January 23) at the Veneto region, while the bottom left- and right-hand panels are 2D and 3D reconstructions of a night (2020 February 2) with dense fog on the Po Valley and clear conditions at the Ekar Observatory. Fig. 11 shows how the contribution of the Po Valley is shielded by the fog. The scale and the colour bar are the same as Fig. 1 (700 × 550 pixels

[5] http://www.oapd.inaf.it

Table 3. Main cities contributing to ALAN at Ekar Observatory. The model for an $AOD_{Sat} = 0.2$, particle mean radius = 1.2 μm, zenith angle = 5°, and the observation wavelength $\lambda = 500$ nm provides a magnitude of 20.77 at Ekar Observatory.

City	P	T	D	h	Δh	Radiance	Contribution
	N	N_1	(km)	(m)	(m)	$\left(\frac{nW}{m^2\ sr}\right)$	%
Padua	210 000	16 000	55	12	1354	40.5	6.8
Venice	265 000	20 200	74	1	1365	29.9	5.0
Verona	260 000	19 800	64	59	1307	38.7	6.5
Vicenza	115 000	88 000	34	39	1327	53.3	8.9
Schio	40 000	3100	22	200	1166	42.7	7.2
Thiene	25 000	1900	17	147	1219	41.7	7.0
Bassano	45 000	3400	15	129	1237	93.4	15.7
Marostica	14 000	1100	13	103	1263	37.3	6.2
Gallio	2500	200	5	1093	273	76.0	12.7
Asiago	6500	500	5.5	1001	365	143.3	24.0

Note. Ekar Observatory Model NSB = 20.77 mag arcsec^{-2}.

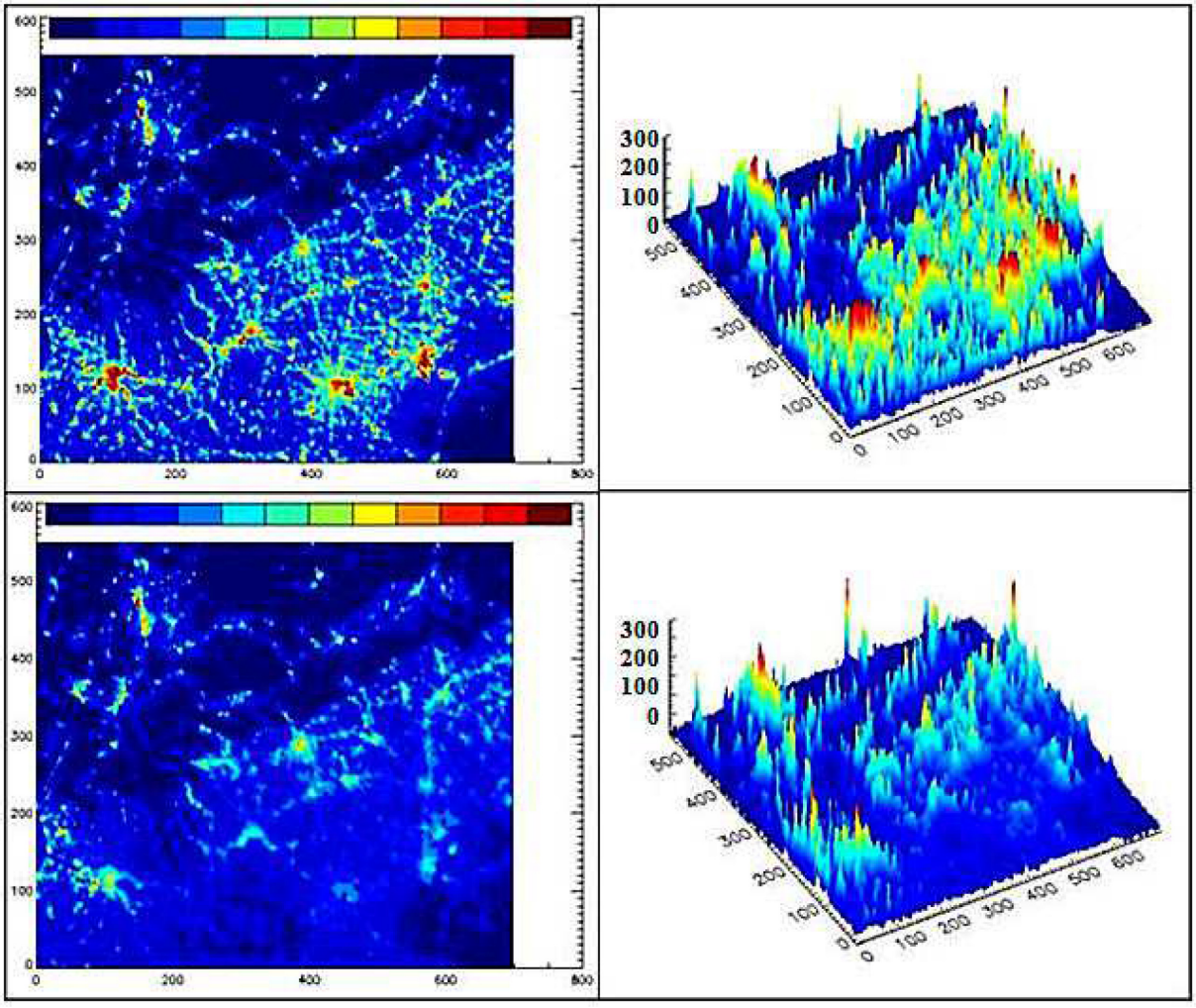

Figure 11. VIIRS data 2D (top left-hand panel) and 3D (top right-hand panel) reconstruction of a clear night (2020 January 23) at the Veneto region compared to a 2D (bottom left-hand panel) and 3D (bottom right-hand panel) reconstruction of a night (2020 February 2) with dense fog on the Po Valley and clear conditions at the Ekar Observatory. Figure shows how the contribution of the Po Valley is shielded from the fog.

corresponding to 140 × 110 km). Fig. 12 shows the comparison between the Padua and Ekar Observatory SQM ground during the clear night represented in the top panels of the Fig. 11 (2020 January 23). Fig. 13 reproduces the ground SQM trends of Padua and Ekar Observatory during the night represented in the bottom panels of the Fig. 11 (2020 February 2). The fog illuminated from below leads to a decrease in ground SQM magnitude on the Padua site, while the Po Valley contribution shielding increases the ground SQM magnitude

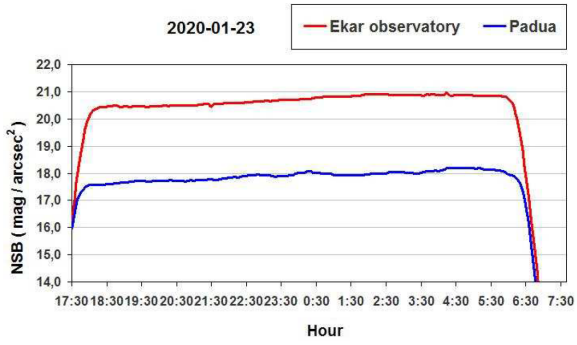

Figure 12. Comparison between the trends of the night SQM measurements (2020 January 23) at Ekar Observatory and at Padua during a clear night in standard conditions.

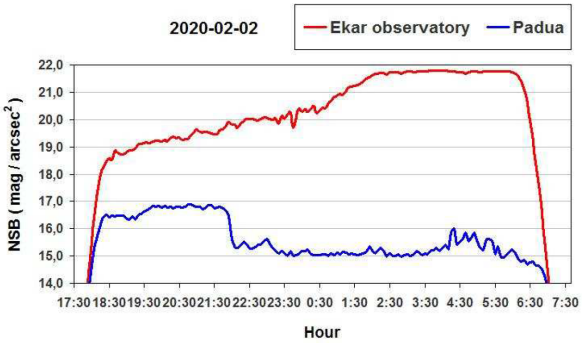

Figure 13. Comparison between the trends of the night SQM measurements (2020 February 2) at Ekar Observatory and at Padua. Figure shows that the dense fog at low altitude decreases the magnitude at Padua and increases the magnitude at Asiago shielding the Po Valley ALAN contribution.

up to 21.79 at Ekar Observatory, with a gain of about 1.0 mag. Table 4 simulates this situation considering only the sources visible from satellite: Schio, Gallio, and Asiago. The model gets a magnitude of 21.72 for the Ekar Observatory. A second verification is provided by a public event to raise awareness of the light pollution issue. On 2014 March 28 the event took place the 'dark night' of the Asiago plateau. The municipality of Asiago turned off the public light (100 per cent) and invited private individuals to turn-off all unnecessary night lights.

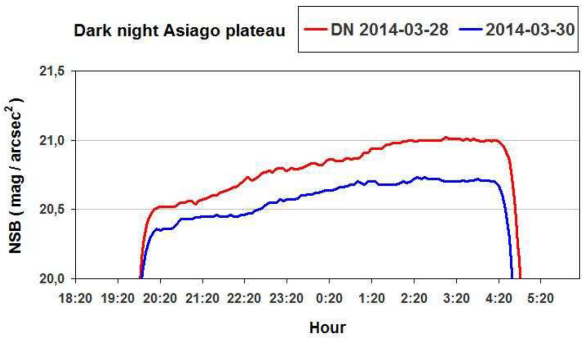

Figure 14. Comparison between the night SQM trends measurements at Ekar Observatory of the 'dark night' initiative (2014 March 28) with a common night (2014 March 30). Figure shows the ALAN contribution of the Asiago plateau.

Fig. 14 compares the SQM trend of this night with a clear night (2014 March 30) and Table 5 shows the values of this simulation. We put in bold font the contribution in radiance by Gallio and Asiago reduced of 50 per cent. The reduced radiance contribution brings the magnitude at Ekar Observatory to a value of 20.99. We conclude our analysis with a triple long-term comparison of three time series. Fig. 15 shows the trend of the monthly averages of the AOD, radiance satellite, and the SQM ground measurements at Ekar Observatory from 2012 to 2019. The radiance data detected by VIIRS ($\left[\frac{nW}{m^2\,sr}\right]$) and the AOD_{Sat} detected by MODIS have been transformed through two simple homoteties respect to the main y-axis (right-hand y-axis). The SQM values are expressed in magnitude ($\left[\frac{mag}{arcsec^2}\right]$) relative to the secondary y-axis (left-hand y-axis). The SQM values are the monthly averages of clear nights over the 2-week period centred on the new Moon to compare them with the satellite data. The VIIRS monthly averages of May, June, and July are not available for the Asiago site. We can see that when the radiance detected by satellite increases the ground SQM measurements decrease, this occurs in most cases in correspondence with an increase of the aerosol concentration. Fig. 4 and Fourier analysis also show that the trend of the AOD is seasonal with an increase in the spring and summer months. The increase of the AOD simultaneously with the new Moon period in clear sky conditions leads to a drop of the VIIRS data count as explained in Section 3. This decrease in satellite counts, due to the radiation blockage caused by the aerosol layer, does not therefore lead to

Table 4. Night with thick fog at low altitude (2020 February 2). The contribution to ALAN of the Po Valley is shielded by fog. The symbol '–' indicates that the city contribution is shielded from the fog. The model simulation for an $AOD_{Sat} = 0.2$, particle mean radius = 1.2 μm, zenith angle = 5°, and the observation wavelength $\lambda = 500$ nm provides a magnitude of 21.72 at Ekar Observatory.

City	P	T	D	h	Δh	Radiance	Contribution
	N	N_1	(km)	(m)	(m)	$\left(\frac{nW}{m^2\,sr}\right)$	(%)
Padua	210 000	16 000	55	12	1354	–	–
Venice	265 000	20 200	74	1	1365	–	–
Verona	260 000	19 800	64	59	1307	–	–
Vicenza	115 000	8800	34	39	1327	–	–
Schio	40 000	3100	22	200	1166	42.7	16.3
Thiene	25 000	1900	17	147	1219	–	–
Bassano	45 000	3400	15	129	1237	–	–
Marostica	14 000	1100	13	103	1263	–	–
Gallio	2500	200	5	1093	273	76.0	29.0
Asiago	6500	500	5.5	1001	365	143.3	54.7

Note. Ekar Observatory Model NSB = 21.72 mag arcsec^{-2}.

Table 5. Dark night on the Asiago plateau. We consider a 50 per cent reduction of the plateau radiance detected by satellite. The model for an $AOD_{Sat} = 0.2$, particle mean radius = 1.2 μm, zenith angle = 5°, and the observation wavelength $\lambda = 500$ nm provides a magnitude of 20.99 at Ekar Observatory.

City	P N	T N_1	D (km)	h (m)	Δh (m)	Radiance $\left(\frac{nW}{m^2\ sr}\right)$	Contribution (%)
Padua	210 000	16 000	55	12	1354	40.5	8.3
Venice	265 000	20 200	74	1	1365	29.9	6.1
Verona	260 000	19 800	64	59	1307	38.7	8.0
Vicenza	115 000	8800	34	39	1327	53.3	10.9
Schio	40 000	3100	22	200	1166	42.7	8.8
Thiene	25 000	1900	17	147	1219	41.7	8.6
Bassano	45 000	3400	15	129	1237	93.4	19.2
Marostica	14 000	1100	13	103	1263	37.3	7.7
Gallio	2500	200	5	1093	273	**37.7**	7.8
Asiago	6500	500	5.5	1001	365	**71.1**	14.7

Note. Ekar Observatory Model NSB = 20.99 mag arcsec^{-2}.

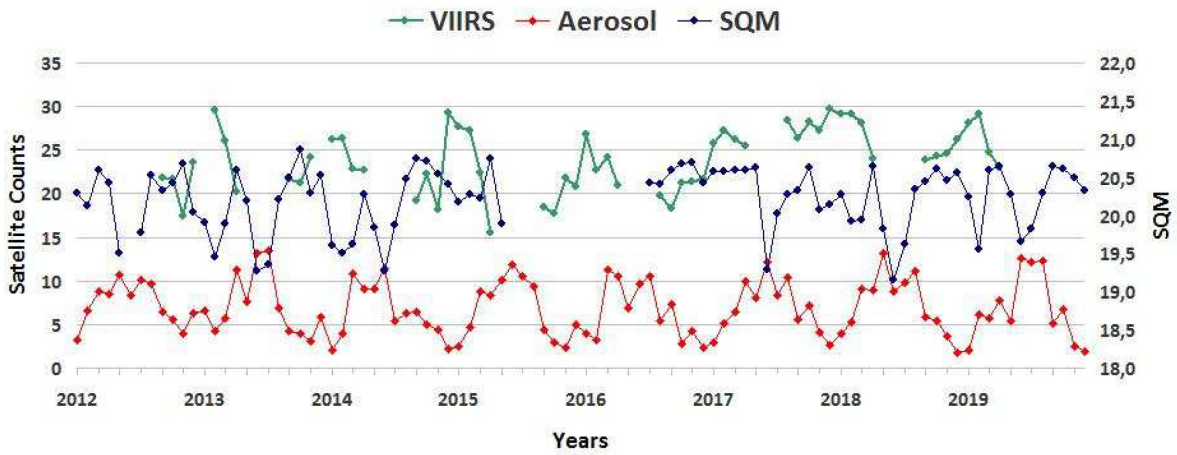

Figure 15. Triple comparison between the aerosol and radiance satellite trends measurements with SQM ground measurements at Ekar Observatory. Figure shows that when the radiance detected by satellite increases the ground SQM measurements decrease, this occurs in correspondence with an increase of the aerosol concentration.

an increase in magnitude from the ground SQM measurements but rather to a decrease.

6 DISCUSSION AND CONCLUSION

In this paper, we analysed the ground light emission detected by satellite from 2012 to 2019 in the Veneto region (see Fig. 1). The satellite time series shows fluctuations, and we explain part of these fluctuations assuming that VIIRS measurements are influenced by lunar cycles in relation to the AOD and the cloud cover (see Figs 2 and 7). We studied the AOD and the cloud cover in the Veneto region from 2003 to 2019 (see Fig. 4). The use of the FFT yields the main periodicities of the two data series with the respective phase. Fig. 5 shows two peaks of cloud cover: the first one every 8.0 d and the second more intense every 8.7 d with the respective phases of +40° corresponding to +21 h and +20° corresponding to +12 h. The same analysis for the AOD shows a peak every 16 d with the relative phase of −20° corresponding to −21 h. The comparison with the ground data made the 8.7-d peak more statistically probable, also confirming the greater amplitude of the oscillation. Fig. 6 shows the empirical analytical model simulation that compares the Moon phases with the periodicities, the maximum and minimum of the cloud cover, and the aerosols in the 2019 first four months. The maximum and minimum are derived empirically from the analysis of satellite data. The model shows the occurrence of four different situations: January full Moon period with cloud cover; February clear full Moon period with high AOD; March clear full Moon period with low AOD; and, finally, April with clear new Moon period with high AOD.

The four situations described above influence satellite measurements by generating fluctuations. The main goal of the paper is to demonstrate that when high aerosol concentration is concurrent with a clear full Moon period the satellite measures an increase in counts (see Fig. 7, February VIIRS radiance, central right-hand panel). This depends on the Moon frontscatter that is created by the system geometry (see Fig. 3). On the contrary, when high aerosol concentration coincides with a period of clear new Moon, the satellite detects a decrease of the counts due to the backscatter from the ground (see Fig. 7, April VIIRS radiance, bottom right-hand panel). The high-resolution photometry of the Asiago municipality shown in Fig. 8 highlights the radial profile trends of the ground emission detected by satellite. The fluctuations are evident in the maximum peak and in the area in the range $5 < r < 10$, where 5 pixels correspond to 1 km. This is because scattering is proportional to the radiance (e.g. the light emission scatters more in the city centre and the immediate periphery).

We also develop an empirical mathematical model of light pollution based on aerosol satellite data. The model considers the ALAN contribution of the main cities in the vicinity of the analysed site, their population and traffic flow, the distance, and the difference in altitude between the city and the observation site. The code works with satellite AOD related to the site altitude, the aerosol particle concentration and radius, as a function of altitude, zenith angle, and observation wavelength. Fig. 10 shows a model simulation with different AOD and aerosol particle radius, as a zenith angle function. We see that the smaller particles scatter the light more efficiently. Table 3 shows the obtained results highlighting the contribution percentage of each city. The model gives a mean magnitude under standard conditions of 20.77 at the Ekar Observatory, showing a 63.3 per cent ALAN contribution from the Po Valley.

We therefore consider two particular situations described in Section 5 to validate the model. Finally, in Fig. 15, we made a triple long-term comparison between the AOD measured by MODIS, the radiance measured by VIIRS, and the SQM ground values. The aerosol concentration fluctuations affect the measurements from the ground and from the satellite. In the second case they can be also influenced by the moonlight in excess or defect. Long-term aerosol concentration decreased from 2003 to 2019 as shown in Fig. 4, the linear regression shows an AOD of 0.34 in 2003 and 0.25 in 2019. Our model described in Section 4 provides a magnitude of 20.58 with the first AOD value and 20.66 with the second value for the Ekar Observatory, this could therefore explain the improvement of the night sky detected by SQM in recent years (Bertolo et al. 2019). The decrease of the aerosols leads to an increase in the magnitude of the sky in an ALAN-contaminated site, but we expect an opposite effect in an uncontaminated site. The particles in a site without ALAN exclusively reduce the natural contribution from above (e.g. fewer particles, brighter sky). We will investigate this effect in a future work.

ACKNOWLEDGEMENTS

This activity is supported by the Istituto Nazionale di Astrofisica (INAF) funds allocated to the Premiale ADONI MIUR. Most of the GOES data used in this paper are from the Comprehensive Large Array-data Stewardship System (CLASS), which is an electronic library of NOAA environmental data. This website provides capabilities for finding and obtaining data, particularly NOAA's Geostationary Operational Environmental Satellite data. MODIS data were provided by the GIOVANNI – Interactive Visualization and Analysis website. We also refer to the 3D atmospheric reconstruction project at Prato Piazza (Italy). We thank astronomer researcher Marina Orio for her careful reading and advice to increase the clarity of this paper. Funding from Italian Ministry of Education, University and Research (MIUR) through the Dipartimenti di eccellenza project Science of the Universe. Finally, we thank the support of the University of Padua for this research (research grant, type A, Rep. 138, Prot. 3022, 26-10-2018).

DATA AVAILABILITY

A part of the data underlying this paper will be shared on reasonable request to the corresponding author while a part of the data are available as described in the paper footnote.

REFERENCES

Aubé M., Kocifaj M., 2012, MNRAS, 422, 819
Aubé M., Simoneau A., 2017, Illumina User's Guide. Available at: https://w1.cegepsherbrooke.qc.ca/ aubema/index.php/Prof/IlluminaGuide2016
Aubé M., Simoneau A., 2018, J. Quant. Spectrosc. Radiat. Transf., 211, 25
Aubé M., Franchomme-Foss L., Robert-Staehler P., Houle V., 2005, in Huang H.-L. A., Bloom H. J., Xu X., Dittberner G. J., eds, Proc. SPIE Vol. 5890, Atmospheric and Environmental Remote Sensing Data Processing and Utilization: Numerical Atmospheric Prediction and Environmental Monitoring. SPIE, Bellingham, p. 248
Aubé M., Fortin N., Turcotte S., Garcia B., Mancilla A., Maya J., 2014, PASP, 126, 1068
Bará S., 2016, R. Soc. Open Sci., 3, 160541
Bará S., Lima R. C., Zamorano J., 2019, Sustainability, 11, 3070
Bertolo A., Binotto R., Ortolani S., Sapienza S., 2019, J. Imaging, 5, 56
Bohren C. F., Huffman D. R., 1998, Absorption and Scattering of Light by Small Particles. Wiley-VCH, Weinheim
Cao C., Wang W., Blonski S., Zhang B., 2017, J. Geophys. Res.: Atmos., 122, 5285
Cavazzani S., Zitelli V., 2013, MNRAS, 429, 1849
Cavazzani S., Ortolani S., Zitelli V., Maruccia Y., 2011, MNRAS, 411, 1271
Cavazzani S., Ortolani S., Zitelli V., 2012, MNRAS, 419, 3081
Cavazzani S., Ortolani S., Zitelli V., 2015, MNRAS, 452, 2185
Cavazzani S., Ortolani S., Zitelli V., 2017, MNRAS, 471, 2616
Cavazzani S., Ortolani S., Scafetta N., Zitelli V., Carraro G., 2019, MNRAS, 484, L136
Cavazzani S., Ortolani S., Bertolo A., Binotto R., Fiorentin P., Carraro G., Saviane I., Zitelli V., 2020, MNRAS, 493, 2463
Cinzano P., 2005, Istituto di Scienza e Tecnologia dell'Inquinamento Luminoso (ISTIL) Internal Report, vol. 1.4, p. 9
Cinzano P., 2007, Istituto di Scienza e Tecnologia dell'Inquinamento Luminoso (ISTIL) ,
Cinzano P., Falchi F., 2012, MNRAS, 427, 3337
Cinzano P., Falchi F., Elvidge C. D., 2001, MNRAS, 328, 689
Coesfeld J., Kuester T., Kuechly H., Kyba C. M., 2020, Sensors, 20, 3287
Cooley J. W., Tukey J. W., 1965, Math. Comput., 19, 297
Cox D. T. C., Sánchez de Miguel A., Dzurjak S. A., Bennie J., Gaston K. J., 2020, Remote Sensing, 12, 1591
Elvidge C. D., Baugh K., Zhizhin M., Hsu F. C., Ghosh T., 2017, Int. J. Remote Sensing, 38, 5860
Espey B., McCauley J., 2014, Lighting Res. Technol., 46, 67
Falchi F. et al., 2016, Sci. Adv., 2, 1600377
Garstang R. H., 1984, The Observatory, 104, 196
Garstang R. H., 1986, PASP, 98, 364
Garstang R. H., 1989, PASP, 101, 306
Garstang R. H., 1991, PASP, 103, 1109
Garstang R. H., 2007, The Observatory, 127, 1
Gaston K., Bennie J., Davies T. W., Hopkins J., 2013, Biological Rev., 88, 912
Hanel A. et al., 2017, J. Quant. Spectrosc. Radiat. Transf., 205, 278
Holker F., Wolter C., Perkin E., Tockner K., 2010, Trends Ecology Evolution, 25, 681
Horvath H., 2014, J. Quant. Spectrosc. Radiat. Transf., 139, 3
Kloog I., Haim A., Stevens R. G., Portnov B. A., 2009, Chronobiology Int., 26, 108
Kocifaj M., 2007, Appl. Opt., 46, 3013
Kocifaj M., 2008, Appl. Opt., 47, 792
Kocifaj M., 2009, Appl. Opt., 48, 4650
Kocifaj M., 2018, J. Quant. Spectrosc. Radiat. Transf., 206, 260
Kocifaj M., Kómar L., 2016, MNRAS, 458, 438
Kyba C. C. M. et al., 2015, Sci. Rep., 5, 8409
Lombardi G., Zitelli V., Ortolani S., Pedani M., Ghedina A., 2008, A&A, 483, 651
Manfrin A. et al., 2017, Frontiers Environmental Sci., 5, 61
Mie G., 1908, Beiträge zur Optik trüber Medien, speziell kolloidaler Metallösungen
Miller S. et al., 2013, Remote Sensing, 5, 6717
Mulder C. et al., 2015, Adv. Ecological Res., 53, 1
Patat F., 2008, A&A, 481, 575
Posch T., Binder F., Puschnig J., 2018, J. Quant. Spectrosc. Radiat. Transf., 211, 144

Pun C. S. J., So C. W., 2012, Environmental Monitoring Assessment, 184, 2537
Puschnig J., Posch T., Uttenthaler S., 2014, J. Quant. Spectrosc. Radiat. Transf., 139, 64
Puschnig J., Wallner S., Posch T., 2020, MNRAS, 492, 2622
Ribas S. J., Torra J., Figueras F., Paricio S., Canal-Domingo R., 2016, Int. J. Sustainable Lighting, 35, 32
Sanchez de Miguel A., Kyba C. C. M., Zamorano J., Gallego J., Gaston K. J., 2020, Sci. Rep., 10, 7829
Schoenberg E., 1929, Theoretische Photometric, Über die Extinktion des Lichtes in der Erdatmosphäre in Handbuch der Astrophysik, Band II, erste Hälfte. Springer. Berlin
Simoneau A., Aube M., Bertolo A., 2020, MNRAS, 491, 4398
Stevens R. G., Brainard G. C., Blask D. E., Lockley S. W., Motta M. E., 2013, Am. J. Preventive Medicine, 45, 343
Treanor P. J., 1973, The Observatory, 93, 117
Zhang J.-C., Fan Z., Yan J.-Z., Bharat Kumar Y., Li H.-B., Gao D.-Y., Jiang X.-J., 2016, PASP, 128, 105004

This paper has been typeset from a TEX/LATEX file prepared by the author.